Elucidating Primary Degradation Mechanisms in High-Cycling-Capacity, Compositionally Tunable High-Entropy Hydrides

Renato Belli Strozi, Matthew Witman, Vitalie Stavila, Jakub Cizek, Kouji Sakaki, Hyunjeong Kim, Oksana Melikhova, Loïc Perrière, Akihiko Machida, Yuki Nakahira, et al.

Elucidating primary degradation mechanisms in high cycling capacity, compositionally tunable high entropy hydrides

Renato Belli Strozi[1,2], Matthew Witman[3], Vitalie Stavila[3], Jakub Cizek[4], Kouji Sakaki[5], Hyunjeong Kim[5], Oksana Melikhova[4], Loïc Perrière[1], Akihiko Machida[6], Yuki Nakahira[6], Guilherme Zepon[2], Walter José Botta[2], Claudia Zlotea[1]*

[1]Univ Paris Est Creteil, CNRS, ICMPE, UMR 7182, 2 rue Henri Dunant, 94320 Thiais, France

[2]Department of Materials Engineering, Federal University of São Carlos, DEMa-UFSCar, 13565-905, São Carlos, Brazil

[3]Sandia National Laboratories, Livermore, California 94551, United States

[4] Faculty of Mathematics and Physics, Charles University, V Holesovickach 2, Prague 8 18000, Czech Republic

[5] National Institute of Advanced Industrial Science and Technology, AIST West, 16-1 Onogawa, Tsukuba, Ibaraki, 305-8569, Japan

[6] National Institutes for Quantum Science and Technology, 1-1-1, Kouto, Sayo-cho, Sayo-gun, Hyogo, 679-5148, Japan

KEYWORDS: multiprincipal element alloys, hydrogen storage, thermodynamics, cycling, pair distribution function, positron annihilation spectroscopy

ABSTRACT

The hydrogen sorption properties of single-phase *bcc* $(TiVNb)_{100-x}Cr_x$ alloys (x = 0-35) are reported. All alloys absorb hydrogen quickly at 25 °C forming *fcc* hydrides with storage capacity depending on the Cr content. A thermodynamic destabilization of the *fcc* hydride is observed with increasing Cr concentration, which agrees well with previous compositional machine learning models for metal hydride thermodynamics. Steric effect or repulsive interactions between Cr-H might be responsible for this behavior. The cycling performances of the TiVNbCr alloy shows an initial decrease in capacity, which cannot be explained by a structural change. Pair distribution function analysis of the total X-ray scattering on the first and last cycled hydrides demonstrated an average random *fcc* structure without lattice distortion at short range order. If the as-cast alloy contains a very low density of defects, the first hydrogen absorption introduces dislocations and vacancies which cumulate into small vacancy clusters, as revealed by positron annihilation spectroscopy. Finally, the main reason of the capacity drop seems to be due to dislocations formed during cycling while the presence of vacancy clusters might be related to the lattice relaxation. Having identified the major contribution to the capacity loss, compositional modifications to the TiVNbCr system can now be explored that minimize defect formation and maximize material cycling performance.

Introduction

The use of hydrogen as a clean energy carrier is a promising solution to decarbonize the energy and industry sectors; however, various technical and materials related obstacles are inhibiting real-world implementation of hydrogen related processes. Among many current barriers, safe and compact hydrogen storage is a well identified bottleneck. Current research trends are focused on increasing the volumetric and gravimetric capacities, improving the reaction rates, and identifying low-cost materials operating at near ambient temperature and pressure [1].

Among material classes that are currently studied for solid-state hydrogen storage, metal hydrides is one of the most promising due to several advantages such as safety (use of moderate gas pressure), reversibility of absorption and desorption reactions, adjustable thermodynamic properties by numerous chemical substitutions, and high volumetric densities (often exceeding the 71 g/L value for liquid hydrogen at 20 K) [2]. Research in this field is very active worldwide, and a new class of alloys called multiprincipal element alloys (MPEAs), composed of several elements in close to equimolar ratios, has been recently proposed to alleviate the drawbacks of traditional materials. High entropy alloys (HEAs) are a subclass of MPEAs that contain at least 5 elements with concentration in the range 5 – 35 at.% [3]. Moreover, the MPEAs/HEAs are known to adopt simple crystalline structures such as, body-centered-cubic (*bcc*), face-centered-cubic (*fcc*) and hexagonal compact (*hcp*). Though still under debate, the thermodynamic stability of such phases seems to be based on several chemical and physical characteristics, such as configurational entropy, enthalpy of mixing, lattice distortion (δ) and valence electron concentration (VEC), as discussed elsewhere [3].

Several MPEAs and HEAs mainly containing refractory elements have been already explored with promising hydrogen storage properties [4,5], and some of the most interesting candidates are

lightweight compositions containing Ti, V, Cr, and Nb [6–8]. Nygård *et al*. first reported on the hydrogen absorption in the equimolar TiVCrNb alloy which can absorb up to 2 hydrogen per metal atom (H/M) forming a dihydride at room temperature with an impressive volumetric hydrogen density of 160 kg/m^3 [6]. The thermodynamic properties of the *fcc* dihydride formation have been previously reported: ΔH_{abs} = -51.6 kJ/mol H_2 and ΔS_{abs} = -129.3 J/(K·mol H_2) [7]. Silva *et al*. calculated the thermodynamic properties of the $(TiVNb)_{85}Cr_{15}$ alloy for the dihydride formation and found the values ΔH_{abs} = -67 kJ/mol H_2 and ΔS_{abs} = -172 J/(K·mol H_2) [9]. These values are quite different from the equimolar alloy reported by Nygård *et al*. [7] and more closer to the ternary TiVNb alloy reported by Pineda-Romero *et al*. [10]. However, these results are scattered since they focus on individual alloys without a systematic approach. Recently, Strozi *et al*. conducted the first methodical study to highlight the effect of Cr concentration in the Ti-V-Cr-Nb system [8,11]. In this first report, the authors clearly demonstrated that the equilibrium pressures in the Pressure-Composition-Isotherms (PCI) at room temperature can by tuned by modifying the Cr amount. The increase of Cr from 15 to 35 at. % into $(TiVNb)_{100-x}Cr_x$ progressively raises the equilibrium pressure of the dihydride formation suggesting that the thermodynamic properties of the hydrogen absorption reaction can be tuned by adjusting the Cr composition [8]. Later, the thermodynamic properties of two Cr-rich compositions have been determined: ΔH_{abs} = -49 kJ/mol H_2 and ΔH_{abs} = -39 kJ/mol H_2 for $(TiVNb)_{70}Cr_{30}$ and $(TiVNb)_{65}Cr_{35}$, respectively [11]. These previous experimental reports have demonstrated that altering the Cr content in the $(TiVNb)_{100-x}Cr_x$ system strongly affects the thermodynamics of the dihydride formation. However, a systematic approach to clarify the effect of Cr in $(TiVNb)_{100-x}Cr_x$ system on both the structural and thermodynamic properties has not yet been proposed.

In addition to essential performance properties of hydrides such as capacity and thermodynamics, another very important and less studied property is the cycle life stability during absorption/desorption sequences. Diminishing reversible capacity during absorption/desorption cycles is a widely observed phenomenon in metal hydrides, irrespective of material class (e.g., intermetallics, alloys, or complex hydrides). Both extrinsic and intrinsic factors are commonly attributed to this degradation in performance. The most well-known extrinsic factors are impurities in the H_2 gas and vacuum contaminants that can poison the alloy's surface by either oxidation or adsorption of hydrocarbons. Intrinsic factors often include the following (*i*) disproportionation *via* the formation of thermodynamically stable hydrides [12], (*ii*) progressive cumulation of chemical inhomogeneities leading to phase segregation, (*iii*) kinetic issues leading to incomplete absorption or desorption, (*iv*) decrease in the degree of crystallinity [13], and (*v*) extensive amorphization [14]. For more details on the life cycle stability of several reported high entropy alloys with regards to both intrinsic and extrinsic factors we recommend several recent reviews [4,15].

Thus, the aim of the present study is to unravel trends in the hydrogen sorption properties of the $(TiVNb)_{100-x}Cr_x$ series as a function of the Cr content for a wide range of compositions. Along with the thermodynamic properties of dihydride formation as function of Cr content, we will also tackle other parameters such as the maximum (saturation) capacity, desorption behaviour, and cycling properties. For an in-depth understanding of the role of Cr in this system, we will assemble earlier findings from the ternary TiVNb (x = 0) [10], the quaternary $(TiVNb)_{100-x}Cr_x$ alloys with x = 25, 30, 35, and 40 [9,11,16] alongside with new compositions with x = 15 and 20. Cycling effects will be addressed with the help of advanced experimental techniques such as, positron annihilation spectroscopy and pair distribution function analysis of synchrotron X-ray scattering.

Materials and methods

The $(TiVNb)_{100-x}Cr_x$ alloys with x = 15, 20, 25, 30 and 35 at.% Cr were synthesized by high temperature arc melting under Ar atmosphere, as previously reported [9–11,16]. The samples were turned and remelted at least five times to enhance the chemical homogeneity. The as-cast materials were further studied without further annealing since solid solutions are expected to form under non-equilibrium solidification conditions due to rapid cooling rates of the arc-melting method. On the contrary, annealing is susceptible to produce multi-phase samples under conditions closer to the thermodynamic equilibrium than those from arc-melting, as recently demonstrated for refractory high entropy alloys [17].

Structural characterizations were carried out by X-ray powder diffraction by the help of a D8 advance Bruker diffractometer (Cu K_α radiation, Bragg–Brentano geometry). The X-ray powder diffraction data were refined using the Rietveld method with Fullprof software [18].

Hydrogen sorption properties were determined by measuring the absorption kinetic curves at room temperature, the Pressure–Composition Isotherms (PCI) at several temperatures (in the range 100 - 150 °C) and the absorption/desorption cycling by the help of homemade volumetric instruments with thermostatically calibrated volumes. The samples were loaded in a stainless-steel container and activated by a heat treatment at 450 °C under dynamic vacuum for at least 3 hours. For the calculation of the hydrogen uptake, the real equation of state for hydrogen was used from the program GASPAK V3.32 (Cryodata. Inc., Boulder, CO, USA). The kinetic measurements have been performed under a final hydrogen pressure of 33 bar at 25 °C. The absorption/desorption cycling have been carried out by a sequence of absorption at 33 bar and 25 °C followed by desorption of the hydride by heating to 450 °C (7.5 °C/min) under dynamic vacuum (10^{-5} mbar) in the volumetric apparatus, and finally cooling to room temperature.

The hydrogen desorption profile was recorded by thermal desorption spectroscopy (TDS) using a homemade instrument equipped with a quadrupole mass spectrometer (QMS), as described elsewhere [19]. The procedure consists of loading 15 mg of the hydride sample and measuring the evolved gases by the QMS working under secondary vacuum (10^{-6} mbar) during constant heating rate (5 °C/min). During loading into the instrument, all powder samples have been air-exposure but, this was systematically limited to few minutes.

Synchrotron X-ray total scattering experiments were carried out at BL22-XU at SPring-8 synchrotron for pair distribution function (PDF) analysis in real space. The detailed experimental procedure for synchrotron X-ray is given elsewhere [13,14,20]. The samples in fine powder were loaded into a kapton capillary with 1.0033 mm diameter and 0.0508 mm wall thickness. A wavelength of 0.178830 Å was used and the signal was truncated at Q_{max} = 18 $Å^{-1}$ because of the unfavourable signal to noise ratio at high-Q regions. The data processing program PDFgetX2 [21] was used to obtain the PDF patterns. Real space modelling of X-ray data was carried out using the PDFgui program [22]. Structural refinement in reciprocal space was carried out by Rietveld analysis using the RIETAN-FP program [23].

Positron annihilation spectroscopy (PAS) was employed for the characterization of lattice defects. Two complementary (PAS) techniques were used: (i) positron lifetime (PL) spectroscopy [24] which enables identification of open volume defects in the samples; and (ii) coincidence Doppler broadening (CDB) [25] which provides information about local chemical environment of defects.

A ^{22}Na radioisotope with an activity of 1 MBq deposited on a 7 μm thick Kapton foil (DuPont) was used as a positron source. For measurement of bulk samples, the positron source was sealed between two pieces of sample. In the case of powder samples, the positron source was placed in the center of a small cylindrical chamber with a diameter of 6 mm and a height of 5 mm.

Subsequently, the chamber was filled with the measured powder and closed. Dimensions of the chamber ensure that virtually all positrons are thermalized inside the chamber and therefore are annihilated in the studied powder.

A digital positron lifetime spectrometer [26] was employed for PL measurements. The spectrometer exhibits time resolution of (145 ± 1) ps (FWHM of resolution function for ^{22}Na). At least 10^7 positron annihilation events were collected in each PL spectra. Decomposition of PL spectra into individual components was performed using a PLRF code, version 19 [27]. The source contribution to PL spectra was determined using a procedure described in Ref. [28] and consisted of two weak components with lifetimes of ≈380 ps and ≈1.9 ns and corresponding intensities of ≈ 13 % and ≈ 0.3 %.

CDB studies were carried out using a digital spectrometer [29] equipped with two high-purity Ge detectors. The energy resolution of the CDB spectrometer is (0.99 ± 0.02) keV at 511 keV. At least 10^8 annihilation events were collected in each two-dimensional γ-ray energy spectrum, which was subsequently reduced into two one-dimensional cuts representing the resolution function of the spectrometer and the Doppler broadened annihilation profile. CDB results are presented as ratio curves with respect to a well annealed pure Al (99.99999 %) reference.

Results and discussion

Chemical composition effect in the $(TiVNb)_{100-x}Cr_x$ series

The lattice distortion (δ) and VEC of the $(TiVNb)_{100-x}Cr_x$ series with x = 0, 15, 20, 25, 30, 35, and 40 are listed in Table 1. The values of the atomic radius for the lattice distortion calculation were taken from the reference [30]. The lattice distortion increases from 4.43 to 6.45 % with Cr content (max 40 %) due to chromium's smallest radius (1.25 Å) among all other elements (1.45,

1.43 and 1.31 Å for Ti, Nb and V, respectively). Thus, increasing the Cr amount raises the atom size disparity in this series of alloys. VEC also increases with the Cr concentration from 4.66 to 5.20.

Cr amount x (at.%)	δ (%)	VEC	Initial phase	a_{bcc} (Å)	Hydride phase	a_{fcc} (Å)	Capacity (H/M)	reference
0	4.43	4.66	*bcc*	3.211(2)	*fcc*	4.443(2)	2.0	[10]
15	5.64	4.86	*bcc*	3.166(3)	*fcc*	4.403(2)	1.91	Present work
20	5.9	4.93	*bcc*	3.156(3)	*fcc*	4.393 (2)	1.93	Present work
25	6.11	5.00	*bcc*	3.132(1)	*fcc*	4.378(2)	1.90	Present work and [7]
30	6.27	5.06	*bcc*	3.115(2)	*fcc*	4.363(2)	1.90	Present work and [11]
35	6.39	5.13	*bcc*	3.099(3)	*fcc+bcc*	4.345(3)	1.76	Present work and [11]
40	6.45	5.20	Multiphase	-	Multiphase	-	0.65	[11]

Table 1. The semi-empirical δ and VEC parameters, the lattice parameters of the initial alloy and the hydride phase for the $(TiVNb)_{100-x}Cr_x$ series with x = 0, 15, 20, 25, 30, 35 and 40.

The XRD patterns of the series of $(TiVNb)_{100-x}Cr_x$ alloys with x = 0, 15, 20, 25, 30, and 35 are shown in Figure 1A. Several samples show a strong preferential orientation along the (200) direction which is often encountered in refractory *bcc* HEAs [31]. The composition with 40 at.% Cr is multiphase with a main C15 Laves intermetallic coexisting with a minor *bcc* phase, as described in reference [8]. This finding confirms the already reported empirical observation that multiphase materials may be obtained for large lattice distortion (δ = 6.45 %) [32]. All alloys with x = 0 - 35 at.% Cr are single-phase *bcc* materials with the unit cell parameters decreasing almost linearly with Cr content (Figure 1B), as expected due to the smaller size of Cr atom compared to the other elements (Ti, V and Nb). Moreover, this trend is consistent with well-known Vegard's law for substitutional solid solutions [33].

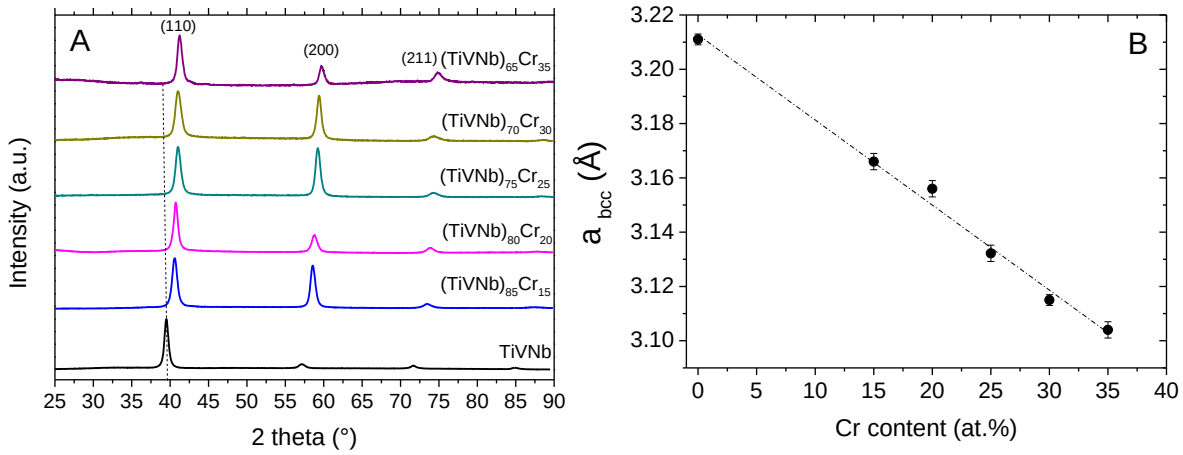

Figure 1. XRD patterns (A) and the variation of the *bcc* lattice parameter as function of Cr content (B) for the series of $(TiVNb)_{100-x}Cr_x$ alloys with x = 0, 15, 20, 25, 30, and 35. The linear fit of the *bcc* lattice parameters as function of Cr content is also plotted as dotted line.

All alloys absorb hydrogen quickly at room temperature under 33 bar hydrogen pressure forming *fcc* (CaF_2-type structure) dihydride phases (as plotted in Figure 2A) with maximum capacities listed in Table 1. The kinetic curves for all samples are shown in Figure SI-1. The *fcc* lattice parameters are given in Table 1 and plotted in Figure 2B *versus* Cr content. The *fcc* lattice parameters linearly decrease with increasing Cr content, in agreement with the reduction of the *bcc* lattice parameter in the as-cast alloys (Figure 1B).

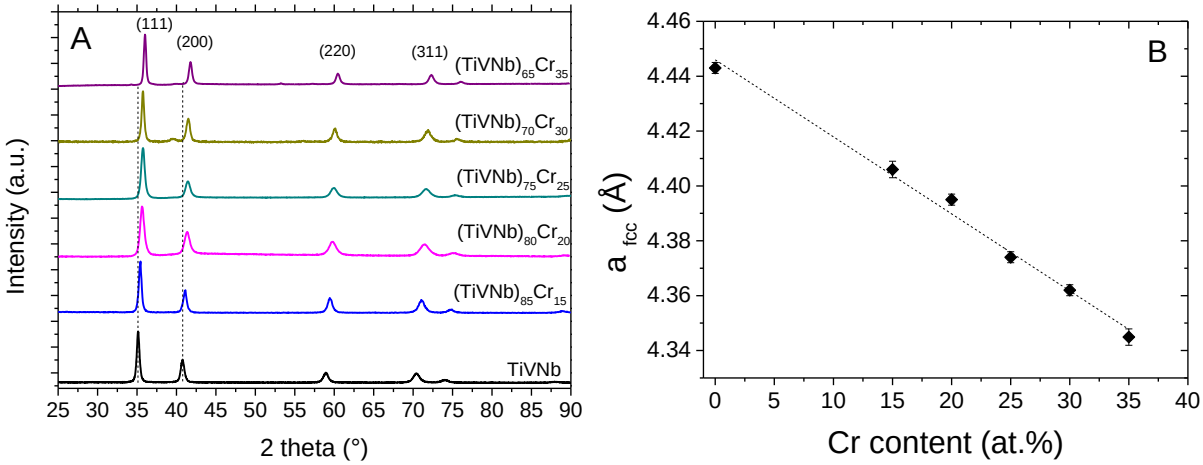

Figure 2. XRD patterns of the dihydrides of $(TiVNb)_{100-x}Cr_x$ alloys with x = 0, 15, 20, 25, 30 and 35 (A) and the corresponding variation of the *fcc* lattice parameter *versus* Cr content (B). The linear fit of the *fcc* lattice parameters is also plotted as dotted line.

The experimentally determined maximum storage capacity slightly decreases from 2.0 to 1.9 with increasing Cr content up to 30 at% followed by a more pronounced drop for higher Cr concentrations (Figure 3). VEC linearly increases with Cr content and the capacity also shows the same qualitative trend with a more noticeable capacity decrease for VEC > 5, in line with previous results for other MPEAs/HEAs systems [6,34]. Interestingly, the same trend can be semi-quantitatively predicted by a machine learning (ML) modeling approach, as shown in Figure 3. Data-driven materials discovery and property prediction, facilitated by ML approaches, is a promising methodology to rationalize the design of novel MPEAs/HEAs from the practically infinite compositional design space [35,36]. The main advantage of these methods is to accelerate the screening and down selection of compositions with desired capacity and thermodynamic properties and therefore reduce the required number of time-consuming experiments. ML predictions in this work correspond to metal hydride capacity and thermodynamics models, trained on v0.0.4 of the ML-ready HydPARK database [37]. Details on model development, validation, and demonstrated

utility for metal hydride discovery are described in Ref.[38]; briefly, we use a compositional ML modelling approach (i.e., use only the composition to generate the materials descriptors [39]) which employs tree-based regressors and interpretability analysis [40] to both predict hydride thermodynamics and elucidate their physically-informed design rules. Ref. [38] also provides the open-source repository to access the code and pre-trained models for community use. The 0 at.% and 25 at.% Cr samples had already been synthesized and measured at the publishing date of the v0.0.4 database and are therefore in the training data. All other compositions represent hold-out predictions for the model. Good quantitative agreement between ML predictions and experimental data is observed for compositions up to 25 at.% Cr. Qualitatively correct prediction of the drop in capacity at high Cr at.% is achieved, although the ML model overestimates the magnitude of this drop for the Cr concentrations 30-35 at.%. The reduced quantitative accuracy of the ML predictions in various compositional regimes is related to the modest number, and significant imbalance, of historically available experimental data that has been collected [35,36]. Nonetheless, these results demonstrate the model's ability to qualitatively, and sometimes quantitatively, *a priori* elucidate the correct compositional design trends in MPEA/HEA hydrides to rationally inform targeted synthesis efforts.

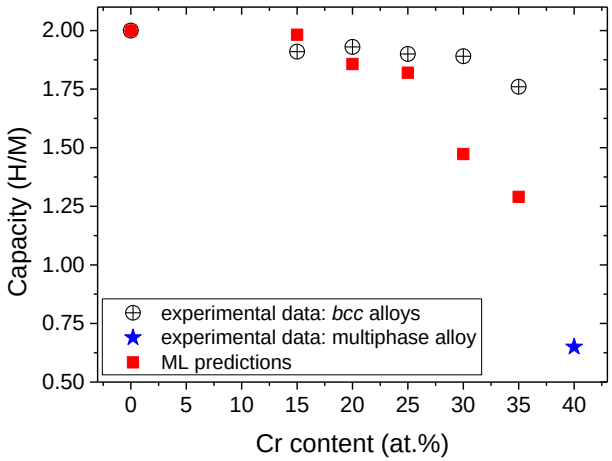

Figure 3. Experimental and ML predicted capacities (H/M) as function of Cr content for hydrides of $(TiVNb)_{100-x}Cr_x$ for x = 0 – 40. The experimental data for *bcc* and multiphase alloys are plotted as circle and star symbols, respectively.

The hydrogen absorption PCI curves for the $(TiVNb)_{100-x}Cr_x$ alloys with x = 15 and 20 at.% Cr are shown in Figure 4. A first transition from the initial alloy to an intermediate monohydride occurs at very low-pressure values (not shown here) followed by a second transformation from the monohydride to a dihydride phase at higher pressure. Only the latter transition is shown in Figure 4 consequently, only thermodynamic information about the formation of the dihydride phase can be extracted from these PCI curves. Applying the van't Hoff method, the enthalpy and entropy of dihydride formation were determined for these alloys and the thermodynamic values are listed in Table 2 together with previously reported results for x = 0 [10], 25 [7], 30, and 35 [11]. The entropy values are higher than the value of H_2 gas entropy, 130 J/K·molH_2, which can be tentatively explained by the slopping nature of the PCI curves.

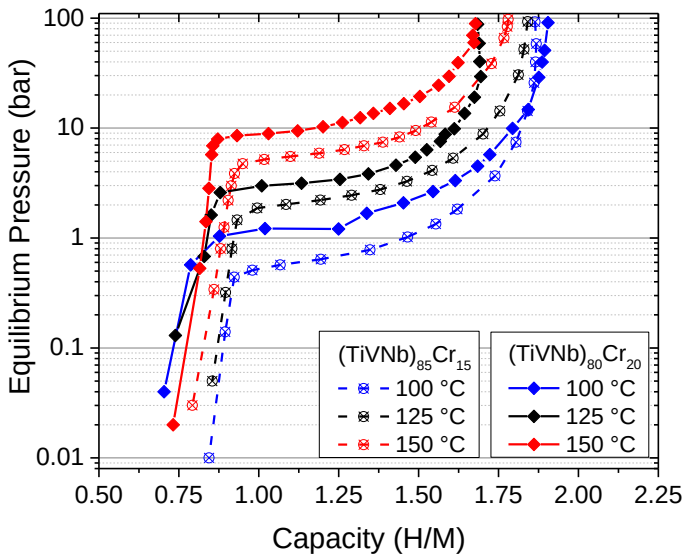

Figure 4. Pressure-Composition-Isotherms for the $(TiVNb)_{100-x}Cr_x$ alloys with x = 15 and 20 at.% Cr.

Sample	Cr amount x (at. %)	Experimental		reference	ML predictions
		Enthalpy (kJ/mol H_2)	Entropy (J/K·mol H_2)		Enthalpy (kJ/mol H_2)
TiVNb	0	-67	-157	[10]	-66.4
$(TiVNb)_{85}Cr_{15}$	15	-57(2)	-151(3)	Present work	-66.2
$(TiVNb)_{80}Cr_{20}$	20	-54(5)	-149(9)	Present work	-55.4
TiVNbCr	25	-51.6	-129.3	[7]	-47.9
$(TiVNb)_{70}Cr_{30}$	30	-49	-154	[11]	-46.6
$(TiVNb)_{65}Cr_{35}$	35	-39	-134	[11]	-44.5

Table 2. The experimental enthalpy and entropy values for the hydride formation in the $(TiVNb)_{100}$-Cr_x series with x = 0 [10], 15, 20, 25 [7], 30, and 35 [11] together with the ML predictions of the enthalpy of hydride formation.

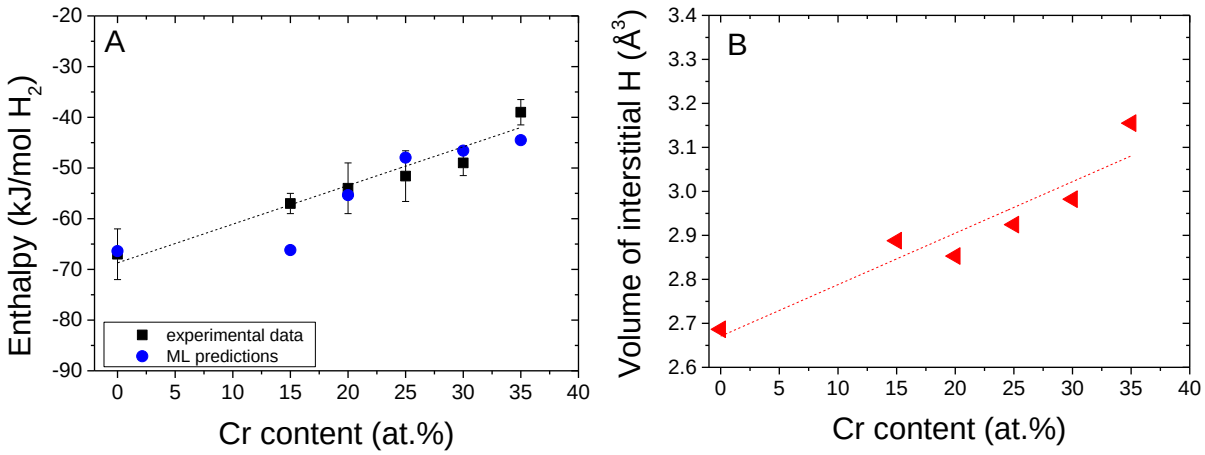

Figure 5. The enthalpy of hydride formation of the $(TiVNb)_{100}$-Cr_x series from both experiments and ML predictions *versus* Cr content (A) and the volume of interstitial hydrogen atom in the $(TiVNb)_{100}$-Cr_x series *versus* Cr content (B). The corresponding linear fits of experimental data are also plotted as dotted lines.

The enthalpy of hydride formation varies almost linearly with Cr content. Cr addition in TiVNb progressively destabilizes the *fcc* hydride which consequently increases the equilibrium pressure

with Cr content, in line with our pervious PCI diagram based on semi-empirical calculations.[9,11] This thermodynamic model predicted a raise of the equilibrium pressure from 10^{-4} bar to 50 bar at 30 °C with the increase of Cr concentration from 10 to 40 at.%. Both experimental and ML predicted values of the enthalpy of hydride formation are plotted as function of the Cr content in Figure 5A. Good correlation can be observed between predictions and experiments, confirming the accuracy of the ML approach for predicting the thermodynamic properties of hydrides of MPEAs, especially since it captures the further destabilization of 30-35 at.% Cr with quantitative accuracy.

Since both thermodynamic (enthalpy of hydride formation) and structural properties (lattice parameters of *bcc* initial phase and *fcc* hydride, Figures 1B and 2B) linearly correlate with Cr content, it is anticipated that thermodynamics also linearly depends on the unit cell volume of the crystalline phase. This hints that the observed thermodynamic destabilization might be related to a steric effect: a smaller available unit cell volume is typically associated with reduced volume of interstitial sites and a larger equilibrium pressure needed to form a hydride phase, and *vice versa*. For example, the same trend is observed in $LaNi_5$ substituted compounds: the increase of the cell volume is accompanied by a decrease of the hydrogen absorption plateau pressure [41]. This trend is yet further consistent with the linear correlation between enthalpy and the composition-weighted mean volume per atom that exists broadly across alloy hydride space (e.g., even beyond just for substitutions within the same material) [35,36].

However, not only steric arguments could be invoked to explain the thermodynamic destabilization but also the repulsive character of Cr – H interactions, since Cr only forms a hydride phase at extremely high pressures (around 3-4 kbar at 150 °C) [42,43]. Moreover, the enthalpies of hydride formation among the four elements constituting the studied alloys, Ti, V, Nb and Cr, as

calculated by first-principles calculations are: $\Delta H_{formation}$ = -121.6, -38.4, -47 and +3.3 kJ/mol par metal atom for Ti, V, Nb hydrides with cubic CaF_2 type structure and Cr hydride with NiAs prototype, respectively [44]. The structure prototypes chosen here (CaF_2 and NiAs) were observed experimentally. A simple comparison between these values hints that the enthalpy of Cr hydride formation is positive whereas the values for Ti, V and Nb are all negative indicating different interactions with hydrogen. A positive enthalpy of formation points out to a thermodynamically unstable phase and consequently, to a repulsive Cr - H character. This trend is illustrated in Figure 5B representing the volume of interstitial hydrogen atom $\left[(\frac{V_{fcc}}{M} - \frac{V_{bcc}}{M})/capacity\ (\frac{H}{M})\right]$ as function of Cr content. These values increase almost linearly from 2.7 to 3.15 $Å^3$ and agree well with the 2.9 $Å^3$ proposed by Peisl [45] for the increase of the volume of the crystal by the addition of one hydrogen atom, irrespective of the material. However, the linear trend observed presently is more surprising since it hints that the volume occupied by one interstitial hydrogen atom increases with Cr concentration suggesting a repulsive nature of Cr – H interactions.

Thermal-desorption properties of the *fcc* hydrides $(TiVNb)_{100-}Cr_x$ (x = 0 – 35 at.%) were measured by applying a heating rate of 5 °C/min under vacuum (Figure 6). The hydrogen desorption involves the complete desorption events from the dihydride to the intermediate monohydride and subsequently to the fully desorbed phase, as already discussed previously [9]. Overall, Cr addition decreases both the onset temperature of desorption and the temperature of maximum desorption rate, and this effect is more pronounced for high Cr content (30 and 35 at.%). This trend is in good agreement with the thermodynamic destabilization of the *fcc* hydride observed experimentally with increasing the Cr amount in $(TiVNb)_{100-x}Cr_x$.

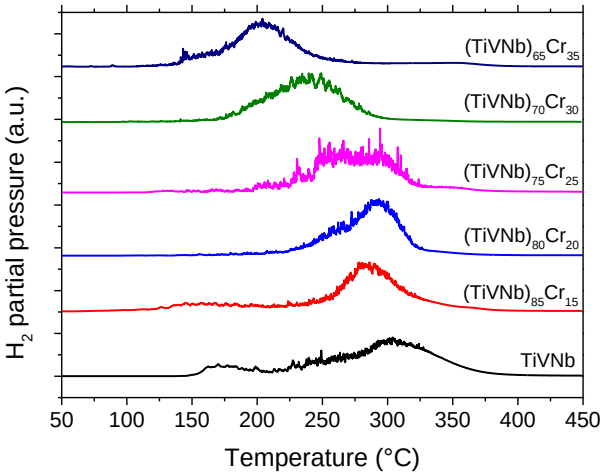

Figure 6. Thermo-desorption spectra for the $(TiVNb)_{100-}Cr_x$ series from x = 0 - 35 at.% Cr recorded in the same instrument with a heating ramp of 5 °C/min.

In conclusion, tuning Cr content in the TiVNb pristine material permits control of the lattice parameters of the as-cast alloys and hydrides, the storage capacity, and the thermodynamic properties of the *fcc* hydride phase as well as its thermal stability.

Cycling effect in the equimolar TiVNbCr alloy

Another very important property of hydride forming alloys is the cycle-life stability during absorption/desorption cycling in terms of crystalline structure, kinetics of reaction, and reversible capacity. These aspects will be developed here on only one composition, the equimolar TiVNbCr (x = 25at.% Cr) alloy, since it has a high initial capacity of 1.9 H/M.

After the first hydrogen absorption, ten absorption/desorption cycles were performed. The changes in reversible capacity upon cycling are shown in Figure 7A and the synchrotron XRD patterns of the hydride phases after the first and the last cycles are presented in Figure 7B. A small

amount of a secondary phase is visible at around 4.4 ° (marked with star in Figure 7B) which is stable with cycling.

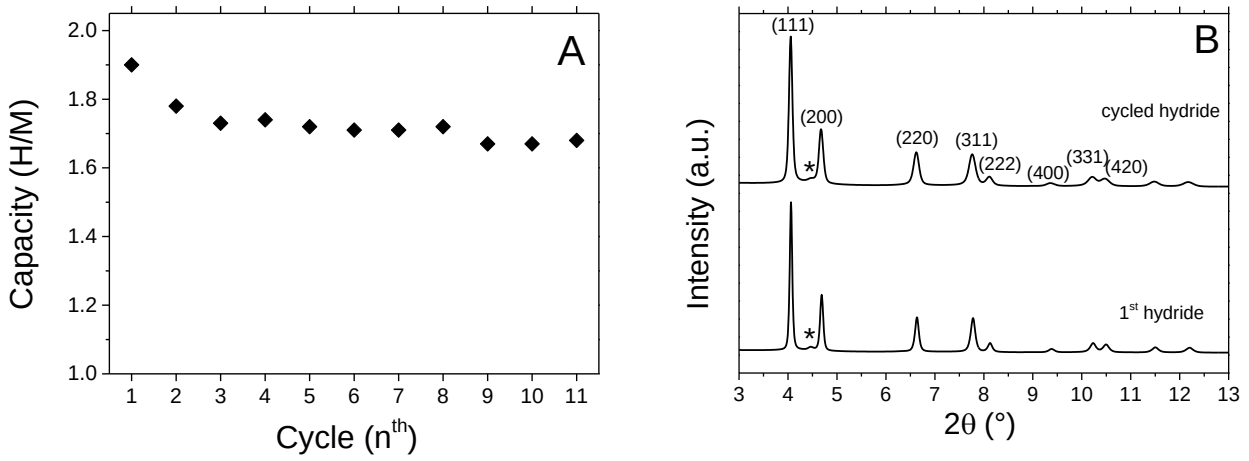

Figure 7. The variation of the capacity (H/M) during several absorption/desorption cycles (A) and the synchrotron XRD patterns (λ = 0.178830 Å) of the *fcc* hydride phase after the first and the last cycle (B). A small amount of a secondary phase is visible at around 4.4 ° and marked with star.

The capacity progressively diminishes in the first 5 cycles from 1.9 to 1.7 H/M (corresponding to around 11 % of the initial capacity) followed by stabilization upon further cycling. The observed loss in the reversible capacity of TiVNbCr cannot be accounted for structural transformation nor phase segregation since the XRD patterns are comparable after the first and last cycles (Figure 7B). A two-phase model was used for Rietveld refinements of the XRD patterns of the two hydride samples: a main *fcc* hydride phase coexisting with a small secondary *bcc* phase (a_{bcc} = 3.243(3) Å with 5-6 % phase fraction) corresponding to the monohydride, irrespective of the cycle number. Interestingly, the major/minor phase fraction (95-94%/5-6%) does not change during cycling indicating that the loss of capacity cannot be accounted for an incomplete rehydrogenation of the material under the present experimental conditions. The only visible change in the XRD patterns is a broadening of the diffraction peaks after cycling suggesting the accumulation of lattice strain.

The results of the Rietveld refinements of XRD data are listed in Table 3 and the related plots are shown in Figure SI-2.

Due to the complexity of this material, advanced characterization techniques have been applied such as, pair distribution function analysis of total X-ray scattering and positron annihilation spectroscopy. The PDF profiles from synchrotron XRD data are shown in Figure 8 for the two hydrides after the first and the last absorption cycles as well as the desorbed phase (first desorption).

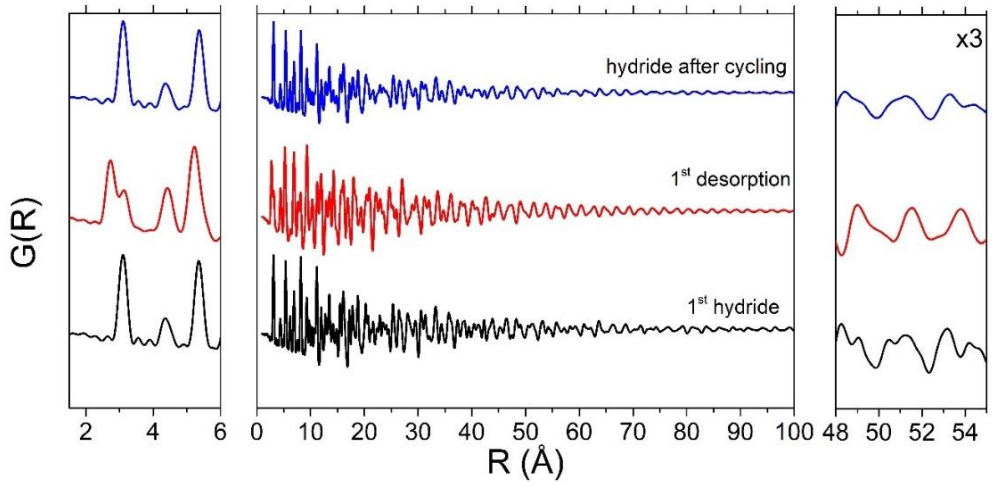

Figure 8. PDF profiles from synchrotron XRD data together with the low-*R* (1.5-6 Å) and high-*R* (48-55 Å) regions for the hydride phase after the first cycle (black), the alloy after the first desorption (red), and the hydride after cycling (blue).

The results of the structural refinements of PDF profiles (lattice parameter and isotropic atomic displacement) are listed in Table 3 and the related plots are shown in Figure SI-3.

Sample	Structure	Capacity (H/M)	From Rietveld		From PDF		
			Lattice parameter (Å)	B (Å²)	Lattice parameter (Å)	B (Å²)	Q_{broad} (Å^{-1})
1st hydride TiVNbCr	*fcc*	1.90	4.3723(1)	0.458(5)	4.3719(3)	0.57(1)	0.052(1)
1st desorbed phase TiVNbCr	*bcc*	-	3.1330(1)	0.83(1)	3.1335(2)	0.96(2)	0.051(1)
cycled hydride TiVNbCr	*fcc*	1.68	4.3820(1)	0.430(6)	4.3807(5)	0.61(2)	0.071(2)

Table 3. Structural refinements details of XRD data and PDF profiles for the *fcc* hydrides after the first and the last absorption cycle as well as the *bcc* phase after the first desorption: structure, lattice parameters and isotropic atomic displacement (B) from both Rietveld and PDF methods as well as Q_{broad} parameter from PDF refinements.

The PDF profiles show the presence of peaks up to 100 Å which proves a long-range structure correlation, irrespective of the state of the alloys (first hydride, desorbed phase or cycled material). The PDF profiles of the hydrides after the first and the last cycles are similar proving that the *fcc* lattice is maintained after cycling, in agreement with the average structure. The main change in the PDF profile introduced by cycling is a *R*-dependent peak broadening responsible for a decrease of the peak's amplitude in the whole *R* range with the largest impact in the high *R* range and significant peak broadening with increasing *R*. This highlights a decrease of the structural correlation in the cycled material as compared to the hydride after the first cycle.

Contrary to the Rietveld refinements of the XRD patterns, the fit of the PDF profiles of the two hydride samples were performed using only one *fcc* phase, irrespective of the cycle number. The refined *fcc* lattice and the isotropic atomic displacement parameters are consistent with those from the Rietveld method (Table 3). The first and the second PDF peaks for the desorbed sample are clearly spitted and the fitting of PDF profile using *bcc* model reproduced well the experimental data. The small difference between the experimental and calculated PDF profiles (Figure SI-3)

demonstrates that the local and medium structures (low-*R* and high-*R* regions) can be well described by undistorted random *fcc* and *bcc* lattices for the two hydride samples and the desorbed phase, respectively. All observed features in the PDF data are well explained by average random structures without any sign of strong lattice distortion at short range order nor elemental segregation introduced by cycling. This result is in agreement with recent reports proving negligible lattice distortion in other CaF_2-type hydrides of HEAs [46,47] and related *bcc* V-Ti-Cr alloys [20].

Moreover, the refined Q_{broad} parameter increases from 0.052 to 0.071 $Å^{-1}$ from the first hydride to the cycled material. Among experimental resolution effects, this parameter has been applied earlier to reproduce the effect of dislocations on the PDF profile [13]. Therefore, an increased Q_{broad} parameter suggests an increased number of dislocations introduced by cycling. Consequently, it seems that intrinsic factors, such as the formation of defects by cycling, might be responsible for the diminishing capacity in the first cycles rather than extrinsic ones.

To gain further understanding in the defect's formation by cycling, we have performed positron lifetime (PL) measurements and coincidence Doppler broadening (CDB) spectroscopy on three samples: the as-cast alloy, the hydrides after the first and the last cycles. The PL experiments provides information about the type and the concentration of the open volume defects present in the sample while CDB enables characterization of the local chemical environment of defects. The results of the PL analysis are collected in Table 4.

Sample	**Capacity (H/M)**	**τ_1 (ps)**	**I_1 (%)**	**τ_2 (ps)**	**I_2 (%)**
As-cast TiVNbCr	-	143.4(2)	100	-	-
1st hydride TiVNbCr	1.90	181(1)	87(1)	340(7)	13(1)
cycled hydride TiVNbCr	1.68	180(3)	68(3)	326(6)	32(2)

Table 4. Results of the PAS analysis: lifetimes τ_i and relative intensities I_i of the exponential components resolved in the PL spectra.

The as-cast sample (TiVNbCr) exhibits a single component spectrum with lifetime of 143 ps that can be accounted by the free positrons delocalized in the *bcc* lattice. Previous results on as-cast MPEAs/HEAs demonstrated the presence of two components in the positron lifetime spectra [48,49]. The short-lived component can be attributed to free positrons (not trapped at defects) while the longer one represents the contribution of positrons trapped in defects, either in dislocations introduced by cutting from ingots [43] or in vacancies introduced by quenching from elevated temperatures [49]. In contrast, the as-cast TiVNbCr alloy shows only one component from free positrons indicating that this material contains a low density of defects and virtually all positrons are annihilated in the free state.

On the contrary, all hydride samples (first and cycled hydrides) contain two components originating from positrons trapped at defects. The component with lifetime of around 180 ps (τ_1) comes from dislocations while the component with larger lifetime 320-340 ps (τ_2) can be attributed to vacancy clusters. The concentration of defects in both the first and cycled hydrides is so high that all positrons are annihilated in trapped state at defects, either dislocations or vacancy clusters, and the free positron component cannot be resolved in PL spectra (so called saturated positron trapping). Therefore, the first hydrogen absorption cycle introduces dislocations and monovacancies which quickly agglomerate into small vacancy clusters. This behavior is widely recognized to originate from the misfit of the lattice parameters between the several phases formed during the hydrogen absorption/desorption. Since PDF results suggested an unstrained lattice of the first hydride, we hypothesize that vacancy clusters are formed to relax the strain lattice introduced by hydrogen-induced plastic deformations and phase transition.

Similarly, the cycled sample also contains both dislocations and vacancy clusters. However, the higher I_2 intensity of positrons trapped into vacancy clusters clearly points out an increase of the concentration of this type of defects as compared to dislocations introduced after cycling. Taking into consideration that PDF revealed an unstrained lattice, we suggest that the formation of more vacancy clusters by cycling results into the relaxation of the lattice. Moreover, the PDF suggested an increased number of dislocations upon cycling, as compared to the first hydride, in good agreement with PAS findings.

The results of CDB measurements are plotted in Figure 9 as ratio curves related to well annealed pure Al. The CDB ratio curve of the as-cast TiVNbCr alloy can be reasonably described by a superposition of equal contributions of CDB curves measured for reference samples of pure elements Ti, V, Nb, and Cr (solid line in Figure 9).

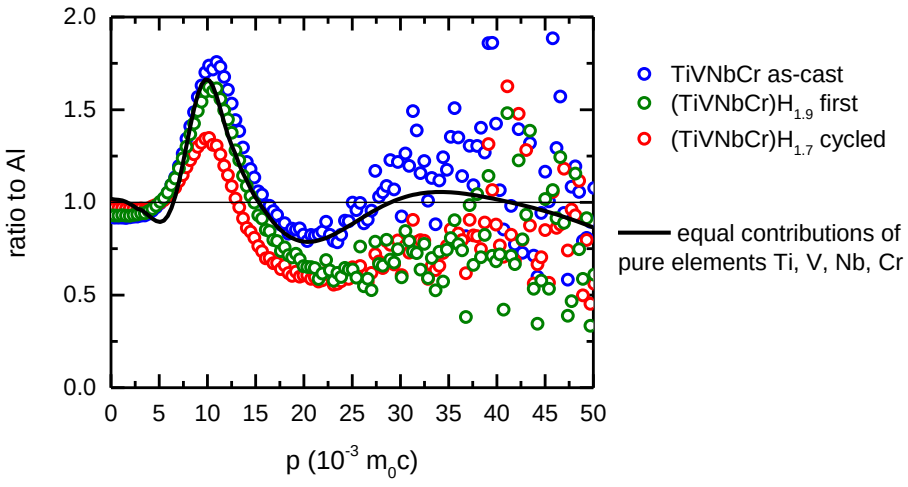

Figure 9. Coincidence Doppler broadening (CDB) ratio curves for the as-cast TiVNbCr (before cycling), the first and cycled hydrides related to pure Al. The solid line shows CDB ratio curve from equal contribution of pure elements (Ti, V, Nb, and Cr).

The CDB ratio curves for samples loaded with hydrogen are suppressed in the high momentum region due to positron localization in hydrogen-induced defects leading to suppressed contribution of positrons annihilated by high momentum core electrons. This effect is more pronounced in the cycled sample which can be reasonably explained by higher concentration of defects, in line with previous PL results. Overall, the chemical environment of defects can be described by a random distribution of Ti, V, Nb, and Cr atoms, irrespective of the sample, in very good agreement with PDF results. Since the dominating contribution arises from positrons trapped at dislocations (intensity 87 and 68% for first and cycled hydride, respectively, see Table 4) the CDB curves reflect mainly the chemical environment of dislocations. However, there is a considerable contribution from positrons trapped in vacancy clusters as well. Random distribution of Ti, V, Nb, and Cr atoms around vacancy seems to be surprising since it has been demonstrated earlier that vacancies in MPEAs/HEAs are preferentially located in the vicinity of atoms with large radii [48,49]. This latter result was, however, obtained for thermally equilibrium vacancies formed in the samples by quenching from high temperatures. Nevertheless, if vacancies are very mobile at high temperatures and can easily find the lowest energy sites in the lattice, vacancy clusters in hydrides studied in the present work were introduced by hydrogen-induced plastic deformations at room temperature. This might explain the random location of formed vacancies in these hydrides.

In light of PDF and PAS results, one possible explanation of the capacity degradation by cycling might be the increasing number of dislocations created during cycling. The interstitial sites in the vicinity of these defects might be heavily distorted and consequently, no longer available for hydrogen occupancy. Having identified the major contributions to the initial drop in cycling capacity, small compositional modifications to the TiVNbCr system can now be explored that minimize defect formation and maximize material cycling performance.

Conclusions

The $(TiVNb)_{100-x}Cr_x$ alloys with x = 0, 15, 20, 25, 30 and 35 are single-phase *bcc* materials with reduced lattice parameter by increasing the Cr content. All alloys absorb hydrogen quickly at room temperature forming *fcc* hydride phases where the maximum storage capacity decreases with increasing Cr amount. The experimental values of enthalpy of hydride formation vary almost linearly with Cr content, in agreement with ML predictions, as well as with the volume of *fcc* hydride / metal atom. The latter trend hints to a thermodynamic destabilization that might be related to a steric effect: the smaller the available lattice volume and volume of interstitial sites, the larger the equilibrium pressure needed to form a hydride phase. The destabilization of the hydride phase with increasing Cr content agrees with the lower thermal stability of the hydride phases observed experimentally.

The cycling of the equimolar TiVNbCr shows a decrease of the capacity by 11% in the first cycles which cannot be accounted by a change in the structure nor a phase segregation. PDF analysis of total scattering X-ray data on the first and cycled hydrides indicates that these materials have an average random *fcc* structure without lattice distortion at short range order or elemental segregation introduced by cycling. The only noticeable effect is a smaller structural correlation in the cycled material as compared to the hydride after the first cycle that can be accounted for by the introduction of defects by cycling. Interestingly, the initial as-cast TiVNbCr alloy contains a low density of defects, as uncovered by PAS. If the first hydrogen absorption introduced dislocations and vacancies which cumulate into small vacancy clusters, the cycling increases the numbers of both types of defects. However, the vacancy clusters concentration increases more than dislocations. The role of vacancy clusters formation might be related to the relaxation of the lattice strain introduced by hydrogen absorption. Thus, the degradation of the capacity after successive

cycling is associated with the increased number of dislocations and heavy distortion of the interstitial sites in the vicinities of the defects which may be no longer available for hydrogen. Due to lengthy experiments needed to measure and characterize cycling's effect on hydrogen capacity, literature data remains relatively scarce and no sufficiently large database (~100s of training examples) has been assembled from which an ML model could readily be trained to predict aspects of capacity degradation. However, recent ML work on automated vacancy prediction [50] could be used in conjunction with hydride thermodynamic ML models discussed here to target high entropy alloys that simultaneously have favorable hydride thermodynamics and a low propensity for vacancy formation and therefore may improve cycling capacity.

These new findings bring important insights into both compositional and cycling effects in a series of multiprincipal element alloys and provide detailed design rules for novel metallic materials with promising properties for hydrogen storage.

Acknowledgments

R.B.S. and C.Z. acknowledge Valérie Lalanne, Olivier Rouleau, Benjamin Villeroy and Fabrice Couturas from ICMPE for technical support. A part of this work was supported by the QST Advanced Research Infrastructure for Materials and Nanotechnology under the remit of "Advanced Research Infrastructure for Materials and Nanotechnology" of the Ministry of Education, Culture, Sports, Science and Technology (MEXT), Japan (Proposal No. JPMXP1222QS0122). The synchrotron radiation experiments were performed using a QST experimental station at JAEA beamline BL22XU, SPring-8, with the approval of the Japan Synchrotron Radiation Research Institute (JASRI) (SPring-8 Proposal No. 2022B3782). We are grateful to Dr. K. Ohwada for his support of the synchrotron radiation experiment at BL22XU,

SPring-8. Sandia National Laboratories is a multi-mission laboratory managed and operated by National Technology and Engineering Solutions of Sandia, LLC., a wholly owned subsidiary of Honeywell International, Inc., for the U.S. Department of Energy's National Nuclear Security Administration under contract DE-NA0003525. The views expressed in this article do not necessarily represent the views of the U.S. Department of Energy or the United States Government.

Supporting Information

Figure SI-1: The kinetic curves for $(TiVNb)_{100-x}Cr_x$ alloys with x = 15, 20, 25, 30 and 35 recorded at room temperature under 33 bar hydrogen pressure.

Figure SI-2. Rietveld refinements of synchrotron XRD data for TiVNbCr desorbed (A), $TiVNbCrH_{1.9}$ first hydride (B) and $TiVNbCrH_{1.68}$ cycled hydride (C).

Figure SI-3. PDF refinements for TiVNbCr desorbed (A), $TiVNbCrH_{1.9}$ first hydride (B) and $TiVNbCrH_{1.68}$ cycled hydride (C). The whole *R*-range (1-100 Å) is shown together with the low-*R* region.

AUTHOR INFORMATION

Corresponding Author

*claudia.zlotea@cnrs.fr

Author Contributions

All authors have given approval to the final version of the manuscript.

Funding Sources

This work was financially supported in part by the CAPES- COFECUB cooperation program (process number 88887.627737/2021-00, project number 88887.191910/2018-00).

J.C. and O.M. acknowledge support from the Czech Science Foundation (Grant No. 21-14030S).

This work was supported by Serrapilheira Institute (process number Serra-1709-17362), by the Brazilian National Council Scientific and Technological Development (CNPq grant number 407906/2022-3 and 309467/2021-7), and by the CAPES-COFECUB cooperation program (Coordenação de Aperfeiçoamento de Pessoal de Nível Superior - Brasil) project number: 88887.387428/2019–00).

REFERENCES

(1) Abe, J. O.; Popoola, A. P. I.; Ajenifuja, E.; Popoola, O. M. Hydrogen Energy, Economy and Storage: Review and Recommendation. *Int. J. Hydrog. Energy* **2019**, *44* (29), 15072–15086. https://doi.org/10.1016/j.ijhydene.2019.04.068.

(2) Hirscher, M.; Yartys, V. A.; Baricco, M.; Bellosta von Colbe, J.; Blanchard, D.; Bowman, R. C.; Broom, D. P.; Buckley, C. E.; Chang, F.; Chen, P.; Cho, Y. W.; Crivello, J.-C.; Cuevas, F.; David, W. I. F.; de Jongh, P. E.; Denys, R. V.; Dornheim, M.; Felderhoff, M.; Filinchuk, Y.; Froudakis, G. E.; Grant, D. M.; Gray, E. MacA.; Hauback, B. C.; He, T.; Humphries, T. D.; Jensen, T. R.; Kim, S.; Kojima, Y.; Latroche, M.; Li, H.-W.; Lototskyy, M. V.; Makepeace, J. W.; Møller, K. T.; Naheed, L.; Ngene, P.; Noréus, D.; Nygård, M. M.; Orimo, S.; Paskevicius, M.; Pasquini, L.; Ravnsbæk, D. B.; Veronica Sofianos, M.; Udovic, T. J.; Vegge, T.; Walker, G. S.; Webb, C. J.; Weidenthaler, C.; Zlotea, C. Materials for Hydrogen-Based Energy Storage – Past, Recent Progress and Future Outlook. *J. Alloys Compd.* **2020**, *827*, 153548. https://doi.org/10.1016/j.jallcom.2019.153548.

(3) Miracle, D. B.; Senkov, O. N. A Critical Review of High Entropy Alloys and Related Concepts. *Acta Mater.* **2017**, *122*, 448–511. https://doi.org/10.1016/j.actamat.2016.08.081.

(4) Marques, F.; Balcerzak, M.; Winkelmann, F.; Zepon, G.; Felderhoff, M. Review and Outlook on High-Entropy Alloys for Hydrogen Storage. *Energy Environ. Sci.* **2021**, *14* (10), 5191–5227. https://doi.org/10.1039/D1EE01543E.

(5) Yang, F.; Wang, J.; Zhang, Y.; Wu, Z.; Zhang, Z.; Zhao, F.; Huot, J.; Grobivć Novaković, J.; Novaković, N. Recent Progress on the Development of High Entropy Alloys (HEAs) for Solid Hydrogen Storage: A Review. *Int. J. Hydrog. Energy* **2022**, *47* (21), 11236–11249. https://doi.org/10.1016/j.ijhydene.2022.01.141.

(6) Nygård, M. M.; Ek, G.; Karlsson, D.; Sørby, M. H.; Sahlberg, M.; Hauback, B. C. Counting Electrons - A New Approach to Tailor the Hydrogen Sorption Properties of High-Entropy Alloys. *Acta Mater.* **2019**, *175*, 121–129. https://doi.org/10.1016/j.actamat.2019.06.002.

(7) Nygård, M. M.; Fjellvåg, Ø. S.; Sørby, M. H.; Sakaki, K.; Ikeda, K.; Armstrong, J.; Vajeeston, P.; Sławiński, W. A.; Kim, H.; Machida, A.; Nakamura, Y.; Hauback, B. C. The Average and Local Structure of TiVCrNbDx (X=0,2.2,8) from Total Scattering and Neutron Spectroscopy. *Acta Mater.* **2021**, *205*, 116496. https://doi.org/10.1016/j.actamat.2020.116496.
(8) Strozi, R. B.; Leiva, D. R.; Zepon, G.; Botta, W. J.; Huot, J. Effects of the Chromium Content in (TiVNb)100−xCrx Body-Centered Cubic High Entropy Alloys Designed for Hydrogen Storage Applications. *Energies* **2021**, *14* (11), 3068. https://doi.org/10.3390/en14113068.
(9) Silva, B. H.; Zlotea, C.; Champion, Y.; Botta, W. J.; Zepon, G. Design of TiVNb-(Cr, Ni or Co) Multicomponent Alloys with the Same Valence Electron Concentration for Hydrogen Storage. *J. Alloys Compd.* **2021**, *865*, 158767. https://doi.org/10.1016/j.jallcom.2021.158767.
(10) Pineda-Romero, N.; Witman, M.; Stavila, V.; Zlotea, C. The Effect of 10 at.% Al Addition on the Hydrogen Storage Properties of the Ti0.33V0.33Nb0.33 Multi-Principal Element Alloy. *Intermetallics* **2022**, *146*, 107590. https://doi.org/10.1016/j.intermet.2022.107590.
(11) Strozi, R. B.; Silva, B. H.; Leiva, D. R.; Zlotea, C.; Botta, W. J.; Zepon, G. Tuning the Hydrogen Storage Properties of Ti-V-Nb-Cr Alloys by Controlling the Cr/(TiVNb) Ratio. *J. Alloys Compd.* **2023**, *932*, 167609. https://doi.org/10.1016/j.jallcom.2022.167609.
(12) Tarasov, B. P.; Bocharnikov, M. S.; Yanenko, Y. B.; Fursikov, P. V.; Lototskyy, M. V. Cycling Stability of RNi5 (R = La, La+Ce) Hydrides during the Operation of Metal Hydride Hydrogen Compressor. *Int. J. Hydrog. Energy* **2018**, *43* (9), 4415–4427. https://doi.org/10.1016/j.ijhydene.2018.01.086.
(13) Kim, H.; Sakaki, K.; Ogawa, H.; Nakamura, Y.; Nakamura, J.; Akiba, E.; Machida, A.; Watanuki, T.; Proffen, T. Origin of Degradation in the Reversible Hydrogen Storage Capacity of V1–XTix Alloys from the Atomic Pair Distribution Function Analysis. *J. Phys. Chem. C* **2013**, *117* (50), 26543–26550. https://doi.org/10.1021/jp408766r.
(14) Sakaki, K.; Terashita, N.; Kim, H.; Tsunokake, S.; Majzoub, E. H.; Nakamura, Y.; Akiba, E. Structural Degradation Behavior of Mg2-XPrxNi4 upon Hydrogenation. *J. Alloys Compd.* **2022**, *912*, 165272. https://doi.org/10.1016/j.jallcom.2022.165272.
(15) Kong, L.; Cheng, B.; Wan, D.; Xue, Y. A Review on BCC-Structured High-Entropy Alloys for Hydrogen Storage. *Front. Mater.* **2023**, *10*.
(16) Silva, B. H.; Zlotea, C.; Vaughan, G.; Champion, Y.; Botta, W. J.; Zepon, G. Hydrogen Absorption/Desorption Reactions of the (TiVNb)85Cr15 Multicomponent Alloy. *J. Alloys Compd.* **2022**, *901*, 163620. https://doi.org/10.1016/j.jallcom.2022.163620.
(17) Moussa, M.; Gorsse, S.; Huot, J.; Bobet, J. L. Effect of the Synthesis Route on the Microstructure of HfxTi(1−x)NbVZr Refractory High-Entropy Alloys. *Metals* **2023**, *13* (2), 343. https://doi.org/10.3390/met13020343.
(18) Rietveld, H. M. A Profile Refinement Method for Nuclear and Magnetic Structures. *J. Appl. Crystallogr.* **1969**, *2* (2), 65–71. https://doi.org/10.1107/S0021889869006558.
(19) Zlotea, C.; Chevalier-César, C.; Léonel, E.; Leroy, E.; Cuevas, F.; Dibandjo, P.; Vix-Guterl, C.; Martens, T.; Latroche, M. Synthesis of Small Metallic Mg-Based Nanoparticles Confined in Porous Carbon Materials for Hydrogen Sorption. *Faraday Discuss.* **2011**, *151*, 117–131.
(20) Sakaki, K.; Kim, H.; Majzoub, E. H.; Machida, A.; Watanuki, T.; Ikeda, K.; Otomo, T.; Mizuno, M.; Matsumura, D.; Nakamura, Y. Displacement of Hydrogen Position in Di-Hydride of V-Ti-Cr Solid Solution Alloys. *Acta Mater.* **2022**, *234*, 118055. https://doi.org/10.1016/j.actamat.2022.118055.

(21) Farrow, C. L.; Juhas, P.; Liu, J. W.; Bryndin, D.; Božin, E. S.; Bloch, J.; Proffen, T.; Billinge, S. J. L. PDFfit2 and PDFgui: Computer Programs for Studying Nanostructure in Crystals. *J. Phys. Condens. Matter* **2007**, *19* (33), 335219. https://doi.org/10.1088/0953-8984/19/33/335219.
(22) Juhás, P.; Davis, T.; Farrow, C. L.; Billinge, S. J. L. PDFgetX3: A Rapid and Highly Automatable Program for Processing Powder Diffraction Data into Total Scattering Pair Distribution Functions. *J. Appl. Crystallogr.* **2013**, *46* (2), 560–566. https://doi.org/10.1107/S0021889813005190.
(23) Izumi, F.; Momma, K. Three-Dimensional Visualization in Powder Diffraction. *Solid State Phenom.* **2007**, *130*, 15–20. https://doi.org/10.4028/www.scientific.net/SSP.130.15.
(24) Čížek, J. Characterization of Lattice Defects in Metallic Materials by Positron Annihilation Spectroscopy: A Review. *J. Mater. Sci. Technol.* **2018**, *34* (4), 577–598. https://doi.org/10.1016/j.jmst.2017.11.050.
(25) Lynn, K. G.; MacDonald, J. R.; Boie, R. A.; Feldman, L. C.; Gabbe, J. D.; Robbins, M. F.; Bonderup, E.; Golovchenko, J. Positron-Annihilation Momentum Profiles in Aluminum: Core Contribution and the Independent-Particle Model. *Phys. Rev. Lett.* **1977**, *38* (5), 241–244. https://doi.org/10.1103/PhysRevLett.38.241.
(26) Bečvář, F.; Čížek, J.; Procházka, I.; Janotová, J. The Asset of Ultra-Fast Digitizers for Positron-Lifetime Spectroscopy. **2004**, *539* (1–2), 372–385. https://doi.org/10.1016/j.nima.2004.09.031.
(27) Čížek, J. PLRF Code for Decomposition of Positron Lifetime Spectra. *Acta Phys. Pol. A* **2020**, *137* (2), 177–187. https://doi.org/10.12693/APhysPolA.137.177.
(28) Čížek, J.; Melikhova, O.; Vlasák, T.; Hruška, P.; Starý, D.; Lukáč, F. Characterization of Lattice Distortions in Refractory Metal Complex Concentrated Alloys Using Positron Annihilation Spectroscopy. *Materialia* **2022**, *23*, 101450. https://doi.org/10.1016/j.mtla.2022.101450.
(29) Čížek, J.; Vlček, M.; Procházka, I. Digital Spectrometer for Coincidence Measurement of Doppler Broadening of Positron Annihilation Radiation. *Nucl. Instrum. Methods Phys. Res. Sect. Accel. Spectrometers Detect. Assoc. Equip.* **2010**, *623* (3), 982–994. https://doi.org/10.1016/j.nima.2010.07.046.
(30) Gordon Aylward; Tristan Findlay. SI Chemical Data, 3rd Edition. *J. Chem. Educ.* **1995**, *72* (5), A109. https://doi.org/10.1021/ed072pA109.1.
(31) Zlotea, C.; Sow, M. A.; Ek, G.; Couzinié, J.-P.; Perrière, L.; Guillot, I.; Bourgon, J.; Møller, K. T.; Jensen, T. R.; Akiba, E.; Sahlberg, M. Hydrogen Sorption in TiZrNbHfTa High Entropy Alloy. *J. Alloys Compd.* **2019**, *775*, 667–674. https://doi.org/10.1016/j.jallcom.2018.10.108.
(32) Yang, X.; Zhang, Y. Prediction of High-Entropy Stabilized Solid-Solution in Multi-Component Alloys. *Mater. Chem. Phys.* **2012**, *132* (2), 233–238. https://doi.org/10.1016/j.matchemphys.2011.11.021.
(33) Vegard, L. Die Konstitution der Mischkristalle und die Raumfüllung der Atome. *Z. Für Phys.* **1921**, *5* (1), 17–26. https://doi.org/10.1007/BF01349680.
(34) Zlotea, C.; Bouzidi, A.; Montero, J.; Ek, G.; Sahlberg, M. Compositional Effects on the Hydrogen Storage Properties in a Series of Refractory High Entropy Alloys. *Front. Energy Res.* **2022**, *10*, 991447. https://doi.org/10.3389/fenrg.2022.991447.
(35) Witman, M.; Ling, S.; Grant, D. M.; Walker, G. S.; Agarwal, S.; Stavila, V.; Allendorf, M. D. Extracting an Empirical Intermetallic Hydride Design Principle from Limited Data via

Interpretable Machine Learning. *J. Phys. Chem. Lett.* **2020**, *11* (1), 40–47. https://doi.org/10.1021/acs.jpclett.9b02971.
(36) Witman, M.; Ek, G.; Ling, S.; Chames, J.; Agarwal, S.; Wong, J.; Allendorf, M. D.; Sahlberg, M.; Stavila, V. Data-Driven Discovery and Synthesis of High Entropy Alloy Hydrides with Targeted Thermodynamic Stability. *Chem. Mater.* **2021**, *33* (11), 4067–4076. https://doi.org/10.1021/acs.chemmater.1c00647.
(37) Witman, M.; Allendorf, M.; Stavila, V. Database for Machine Learning of Hydrogen Storage Materials Properties, 2022. https://doi.org/10.5281/zenodo.7324809.
(38) Witman, M.; Sanliang, L.; Bouzidi, A.; Clulow, R.; Chames, J.; Allendorf, E.; Agarwal, S.; Allendorf, M.; Walker, G.; Wadge, M.; Pineda-Romero, N.; Ek, G.; Grant, D.; Sahlberg, M.; Zlotea, C.; Stavila, V. Towards Pareto Optimal High Entropy Hydrides via Data-Driven Materials Discovery. *ChemRxiv Camb. Camb. Open Engage 2022 This Content Prepr. Has Been Peer-Rev.* https://doi.org/10.26434/chemrxiv-2022-wktf4.
(39) Ward, L.; Agrawal, A.; Choudhary, A.; Wolverton, C. A General-Purpose Machine Learning Framework for Predicting Properties of Inorganic Materials. *Npj Comput. Mater.* **2016**, *2* (1), 1–7. https://doi.org/10.1038/npjcompumats.2016.28.
(40) Lundberg, S.; Lee, S.-I. A Unified Approach to Interpreting Model Predictions. arXiv November 24, 2017. https://doi.org/10.48550/arXiv.1705.07874.
(41) Joubert, J.-M.; Charton, J.; Percheron-Guégan, A. Investigation of Structural and Hydrogen Absorption Properties in the LaNi5−xPtx–H2 System. *J. Solid State Chem.* **2003**, *173* (2), 379–386. https://doi.org/10.1016/S0022-4596(03)00116-6.
(42) Driessen, A., A.; Sanger, P., P.; Hemmes, H., H.; Griessen, R. Metal Hydride Formation at Pressures up to 1Mbar. *J. Phys.-Condens. Matter* **1990**, *2* (49), 9797–9814. https://doi.org/10.1088/0953-8984/2/49/007.
(43) Dottor, M.; Crivello, J.-C.; Joubert, J.-M. Thermodynamic Modeling of Cr and Cr–H Systems up to High Temperatures and High Pressures. *Int. J. Hydrog. Energy* **2022**, *47* (55), 23293–23309. https://doi.org/10.1016/j.ijhydene.2022.04.245.
(44) Bourgeois, N.; Crivello, J.-C.; Cenedese, P.; Joubert, J.-M. Systematic First-Principles Study of Binary Metal Hydrides. *ACS Comb. Sci.* **2017**, *19* (8), 513–523. https://doi.org/10.1021/acscombsci.7b00050.
(45) Peisl, H. Lattice Strains Due to Hydrogen in Metals. In *Hydrogen in Metals I*; Alefeld, G., Völkl, J., Eds.; Topics in Applied Physics; Springer Berlin Heidelberg: Berlin, Heidelberg, 1978; Vol. 28, pp 53–74. https://doi.org/10.1007/3540087052_42.
(46) Nygård, M. M.; Sławiński, W. A.; Ek, G.; Sørby, M. H.; Sahlberg, M.; Keen, D. A.; Hauback, B. C. Local Order in High-Entropy Alloys and Associated Deuterides – a Total Scattering and Reverse Monte Carlo Study. *Acta Mater.* **2020**, *199*, 504–513. https://doi.org/10.1016/j.actamat.2020.08.045.
(47) Bouzidi, A.; Laversenne, L.; Zepon, G.; Vaughan, G.; Nassif, V.; Zlotea, C. Hydrogen Sorption Properties of a Novel Refractory Ti-V-Zr-Nb-Mo High Entropy Alloy. *Hydrogen* **2021**, *2* (4), 399–413. https://doi.org/10.3390/hydrogen2040022.
(48) Čížek, J.; Vlasák, T.; Melikhova, O. Characterization of Lattice Defects in Refractory Metal High-Entropy Alloy HfNbTaTiZr by Means of Positron Annihilation Spectroscopy. *Phys. Status Solidi A* **2022**, *219* (9), 2100840. https://doi.org/10.1002/pssa.202100840.
(49) Jodi, D. E.; Listyawan, T. A.; Hruska, P.; Cizek, J.; Park, N.; Lee, U. Study of Vacancies in Fex(CoCrMnNi)100-x Medium- and High-Entropy Alloys by Positron Annihilation

Spectroscopy. *Scr. Mater.* **2021**, *194*, 113654. https://doi.org/10.1016/j.scriptamat.2020.113654.
(50) Witman, M.; Goyal, A.; Ogitsu, T.; McDaniel, A.; Lany, S. Materials Discovery for High-Temperature, Clean-Energy Applications Using Graph Neural Network Models of Vacancy Defects and Free-Energy Calculations. ChemRxiv January 6, 2023. https://doi.org/10.26434/chemrxiv-2022-frcns-v2.

Table Of Contents (TOC) graphic